


Article

Electrochemical Investigation of Corrosion of X80 Steel under Elastic and Plastic Tensile Stress in CO₂ Environment

Wei Wu ^{1,*} , Hailong Yin ^{2,3}, Hao Zhang ², Jia Kang ², Yun Li ² and Yong Dan ¹¹ School of Chemical Engineering, Northwest University, Xi'an 710069, China; danyong@nwu.edu.cn² School of Chemical Engineering and Technology, Xi'an Jiaotong University, Xi'an 710049, China; yinhl@shccig.com (H.Y.); upczhang@stu.xjtu.edu.cn (H.Z.); kangjia1009@stu.xjtu.edu.cn (J.K.); yunli@mail.xjtu.edu.cn (Y.L.)³ General Department, Shaanxi Coal and Chemical Industry Group Co., Ltd., Xi'an 710065, China

* Correspondence: wuwe@nwu.edu.cn; Tel.: +86-29-88302632

Received: 23 October 2018; Accepted: 10 November 2018; Published: 14 November 2018



Abstract: An investigation into the electrochemical corrosion behavior of X80 pipeline steel under different elastic and plastic tensile stress in a CO₂-saturated NaCl solution has been carried out by using open-circuit potential, potentiodynamic polarization, electrochemical impedance spectroscopy, and surface analysis techniques. The results show that the corrosion rate of X80 steel first increases and then slightly decreases with the increase of elastic tensile stress, whereas the corrosion rate sharply increases with the increase of plastic tensile stress. Both elastic and plastic tensile stress can enhance steel corrosion by improving the electrochemical activity of both anodic and cathodic reactions. Moreover, compared with elastic tensile stress, plastic tensile stress has a more significant effect. Furthermore, electrochemical reactions for CO₂ corrosion and mechanochemical effect are used to reasonably explain the corrosion behavior of stressed X80 steel in CO₂ environment.

Keywords: pipeline steel; tensile stress; corrosion; potentiodynamic polarization; EIS

1. Introduction

Pipeline has been acknowledged as a very efficient way for long-distance transportation of oil and natural gas due to its advantages of large transport capacity, low cost, and high reliability. With the increasing demand for oil and natural gas around the world, pipeline materials that are able to satisfy the requirements of higher operating pressure, larger diameter and thinner wall thickness have been paid more attention to. Therefore, the low-alloy high-strength pipeline steels like X70 and X80 become the best selection for new pipeline projects in China and some other countries due to their excellent mechanical properties (strength, deformability, and toughness) and the superior weldability of these steels [1]. However, in practice, pipelines have to suffer from severe environment conditions. More specifically, during the oil or natural gas extraction and transmission process, the aggressive impurities, especially carbon dioxide and chlorides, exist in produced oil and gas, and are unable to be completely removed. Such an environment would easily result in severe CO₂ corrosion, which may reduce the service life of the pipeline and lead to the leakage of the pipeline [2]. Many studies so far have focused on corrosion of high-strength pipeline steels in oil and natural gas transportation environments [2–11].

Besides the aggressive medium, pipelines would also be subject to various stress conditions resulting from internal pressure, soil movement, and so on [12], which play an important role in corrosion behaviors. Some research efforts have been devoted to the effect of applied stress on the

corrosion of pipeline steel. Xu and Cheng [12,13] investigated the effect of uniaxial elastic stress and plastic strain on the corrosion of X100 pipeline steel in a near-neutral pH NS4 solution (a simulated soil solution). They discovered that the static elastic stress has little effect on electrochemical corrosion of steel, whereas plastic strain would enhance the steel corrosion by increasing corrosion activity of the steel during plastic deformation. Boven et al. [14] reported that residual stress and applied stress can both accelerate the corrosion process of X65 steel immersed in near-neutral pH NS4 solution. Bao et al. [15] studied the electrochemical behavior of tensile stressed oil tube steel P110 exposed to a brine solution with dissolved CO₂. It was found that tensile stress can improve the surface thermodynamic activity of P110 steels and accelerate the anodic and cathodic reactions. Li and Cheng [16] investigated the corrosion behavior of X70 steel in carbonate-bicarbonate solution, and found that tensile stress enhance the steel dissolution more significantly than compressive stress. Li et al. [17] studied the corrosion of elastic-stressed X70 steel exposed to CO₂- and H₂S-contained brine solutions and the results show that elastic tensile stress has less effect on the corrosion rate of X70 steel. Wang et al. [18] investigated the effect strain on the corrosion behavior of X80 steel in NaCl aqueous solution. The above researches provided valuable results of the synergism of stress and corrosive medium on pipeline corrosion. However, systematic research on corrosion behavior of stressed high-strength pipeline steel in the typical CO₂ corrosion environment is still scarce, especially on the effect of different levels of plastic stress on the corrosion of pipeline steel.

This study aims to investigate the effect of different levels of elastic and plastic tensile stress on the corrosion behavior of the typical high-strength pipeline steel X80 in a CO₂-saturated NaCl solution. The electrochemical characteristics and corrosion rates of X80 steel under different tensile stress were obtained, and the corrosion morphology was observed. The corrosion mechanism, taking account into tensile stress, were analyzed to better understand the corrosion changes of stressed high-strength pipeline steel in a CO₂ environment.

2. Materials and Methods

2.1. Material and Solution

The experimental specimens were cut from a commercial LSAW (longitudinal submerged arc welding) pipe made of X80 steel. Its chemical composition is listed in Table 1. The stress-strain curve of the steel was measured on a rod specimen through an electronic tensile testing machine (HH-YFML-EDC, Sinotest Equipment Co., Ltd., Changchun, China) with a drawing rate of 3 mm/min, as shown in Figure 1. The mechanical parameters of the X80 steel are as follows: Yield strength (σ_{ys}): 640 MPa; tensile strength (σ_b): 743 MPa; and yield-tensile ratio (λ): 0.861. The geometry and size of the sample used in this work is shown in Figure 2. The surface of the specimen was coated by insulating anticorrosive rubber except only 10 mm long surface at the middle part of the sample as the working electrode. Before the electrochemical experiments, the working electrode surface would be polished up to 1200-grit with SiC paper, washed with distilled water and alcohol, and then dried in a desiccator until use.

Table 1. Chemical composition of X80 steel used in this work (wt%).

Steel	C	Si	Mn	P	Nb	Ti	Al	Mo	Ni	Cu	Cr	Fe
X80	0.05	0.22	1.78	0.01	0.055	0.015	0.044	0.26	0.256	0.143	0.03	Bal.

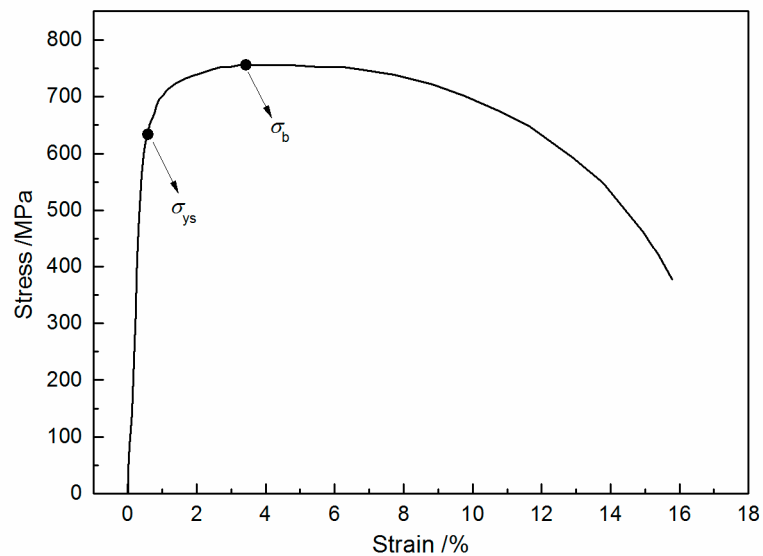


Figure 1. Stress-strain curve of X80 steel at a drawing rate of 3 mm/min in air.

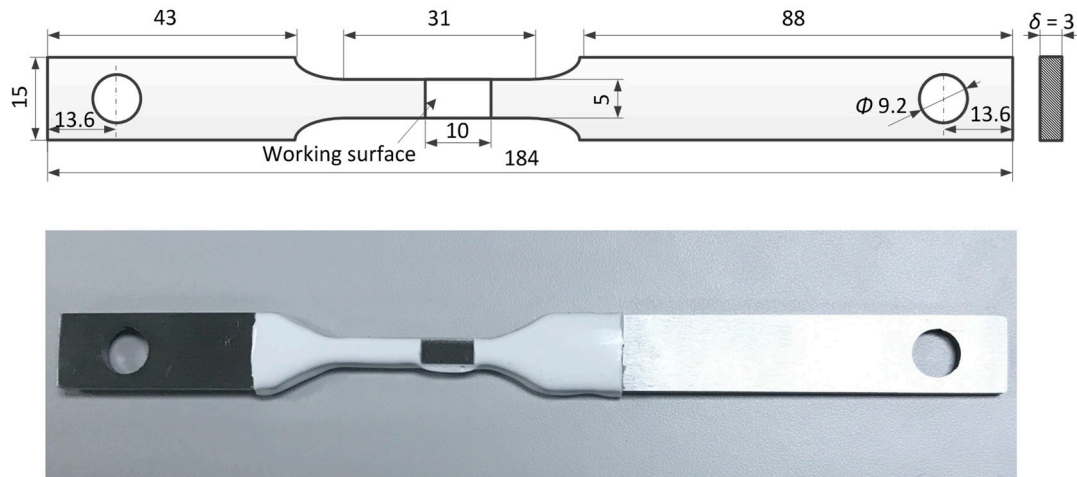


Figure 2. The geometry and the size of the X80 steel specimen (unit: mm).

The specimens were applied with a constant stress at 0%, 30%, 60%, 90%, 103%, 105%, and 108% of its yield strength, respectively. At least three samples were used in each test to avoid accidental error. The electrolyte solution was a 3.5 wt% NaCl aqueous solution (Tianjin Hengxing Chemical Reagent Co., Ltd., Tianjin, China) dissolved with CO₂. To eliminate the influence of oxygen, N₂ was bubbled through the electrolyte to deaerate the aqueous solution for at least one hour. Then, CO₂ was injected at a constant gas flow until the experiment ended. The experimental temperature was controlled to be 30 ± 1 °C during the measurement.

2.2. Experimental Set-Up

The experimental set-up used in this work is shown in Figure 3. It contains an electronic tensile testing machine (HH-YFML-EDC, Sinotest Equipment Co., Ltd., Changchun, China) and a plexiglas-made electrochemical cell. The electrochemical measurements were performed by using a CorrTest CS350 electrochemical workstation (Wuhan Corrttest Instruments Corp., Ltd., Wuhan, China) with a conventional three-electrode system, where the working electrode (WE) is the X80 steel specimen, the reference electrode is a saturated calomel electrode (SCE) and the counter electrode (CE) is a platinum plate.

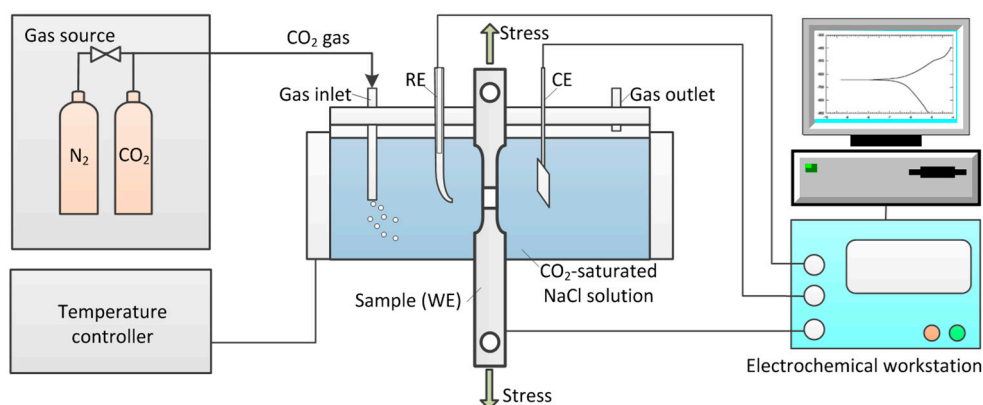


Figure 3. Schematic of the experimental set-up for the electrochemical measurement on the tensile specimen.

2.3. Electrochemical Measurements

The electrochemical methods used in this study include open-circuit potential test (OCP), potentiodynamic polarization scan (PDS), and electrochemical impedance spectroscopy measurement (EIS). The details of each method are described as follows.

OCP refers to the potential in the working electrode comparative to the reference electrode when there is no polarization current or potential existing in the cell. It reflects the electrochemical thermodynamic stability of the steel. The OCP of each specimen was measured from initial immersion to stable value. The measurement time lasted about one hour.

After the stability of OCP, PDS was performed with a scan rate of 0.5 mV/s. The scanning potential range is from -200 mV to 200 mV (vs. OCP). From the potentiodynamic polarization curve, the information of electrochemical kinetics of the steel can be obtained by data fitting.

EIS is one of the widely used electrochemical techniques for studying electrode kinetics of electrode materials due to its non-destructive nature [19,20], from which the electrolyte-electrode interfacial information such as double-layer capacitance, charge-transfer resistance and diffusion impedance can be obtained. In order to investigate the characteristics of electrode reaction of anode and cathode, the EIS would be performed in the weak anodic and cathodic polarization regions, respectively. The optima herefore, in this work, the EIS of each specimen was measured at -60 mV and $+60$ mV (vs. OCP) with the sinusoidal perturbation amplitude of 10 mV and a frequency in the range from 100 kHz to 0.01 Hz.

2.4. Surface Observation

The samples with 90 min of immersion under different tensile stress were examined on a JSM-6390 (JEOL, Akishima, Tokyo, Japan) Scanning Electron Microscope (SEM). The corroded surface morphology of the samples was observed.

3. Results

3.1. Open-Circuit Potential with Time

Figure 4 shows the open-circuit potentials of the X80 steel immersed in 3.5 wt% NaCl aqueous solution with saturated CO₂ under different elastic and plastic tensile stress. It can be seen that the OCP of each sample gradually tends to be a steady-state value with time, though the obvious fluctuation was observed in the beginning of immersion time, which indicates that the X80 steel under different tensile stress reached the thermodynamic stable state. Additionally, in the elastic stress range, the steady-state value of the OCP first decreases and then increases with the increasing tensile stress, while

in the plastic stress range, the OCP monotonously decreases with the increase of tensile stress. Overall, the OCPs of stressed X80 steel are more negative than that without tensile stress.

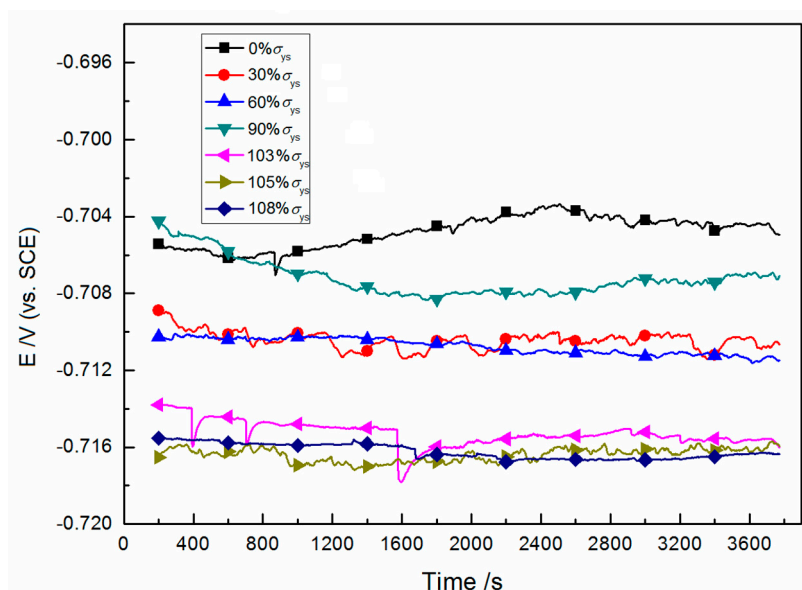


Figure 4. Open-circuit potential of X80 steel in 3.5 wt% NaCl aqueous solution with saturated CO₂ at 30 °C under different elastic and plastic tensile stress.

3.2. Potentiodynamic Polarization

Figure 5 gives the potentiodynamic polarization curves of the tensile stressed X80 steel in 3.5 wt% aqueous solution with saturated CO₂ at 30 °C. The results reveal that all the polarization curves have similar shapes; moreover, there is not an obvious cathodic Tafel region. The anodic Tafel slope of each sample was obtained by fitting the polarization curves, as listed in Table 2.

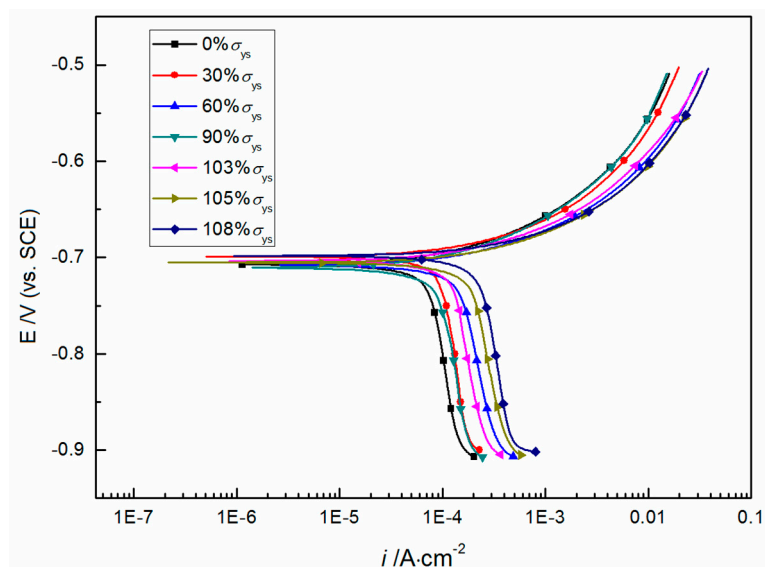


Figure 5. Potentiodynamic polarization curves of X80 steel exposed to 3.5 wt% NaCl aqueous solution with saturated CO₂ at 30 °C under different elastic and plastic tensile stress.

Table 2. Anodic Tafel slope obtained by Tafel fitting of polarization curves for X80 in 3.5 wt% NaCl aqueous solution with saturated CO₂ at 30 °C under different elastic and plastic tensile stress.

Tensile Stress	0% σ_{ys}	30% σ_{ys}	60% σ_{ys}	90% σ_{ys}	103% σ_{ys}	105% σ_{ys}	108% σ_{ys}
$b_a/mV \cdot \text{dec}^{-1}$	40.29	34.54	42.02	35.28	38.52	42.06	39.69

In addition, the corrosion rate of each X80 steel sample in 3.5 wt% NaCl aqueous solution with saturated CO₂ at 30 °C under different tensile stress was calculated based on the corrosion current density through Faraday's law:

$$v_d = 8.76 \times 10^3 \times \frac{i_{\text{corr}} M}{z F \rho} \text{ (mm} \cdot \text{a}^{-1}\text{)}, \quad (1)$$

where M is the molar mass of metal ($\text{g} \cdot \text{mol}^{-1}$), ρ is the density of metal ($\text{g} \cdot \text{cm}^{-3}$), F is the Faraday constant ($96,485 \text{ C} \cdot \text{mol}^{-1}$), and i_{corr} is the corrosion current density ($\text{A} \cdot \text{cm}^{-2}$) and it is obtained by fitting the Tafel curves shown in Figure 5. The calculated results are shown in Figure 6. It is shown clearly that, in the elastic stress range, the corrosion rate increases from $0.845 \text{ mm} \cdot \text{a}^{-1}$ at 0% σ_{ys} to $1.442 \text{ mm} \cdot \text{a}^{-1}$ at 60% σ_{ys} with the increasing tensile stress, and then slightly decreases to $1.110 \text{ mm} \cdot \text{a}^{-1}$ at 90% σ_{ys} . In the plastic stress range, the corrosion rate increases sharply up to $2.631 \text{ mm} \cdot \text{a}^{-1}$ at 108% σ_{ys} , which is about three times higher than that without tensile stress. The change tendency of the corrosion rate is consistent with the observation from OCP. The above results indicate that both elastic and plastic tensile stress can accelerate corrosion reaction rate of X80 steel in the experimental solution, furthermore, plastic tensile stress plays a more important role in the corrosion process, as compared to elastic tensile stress.

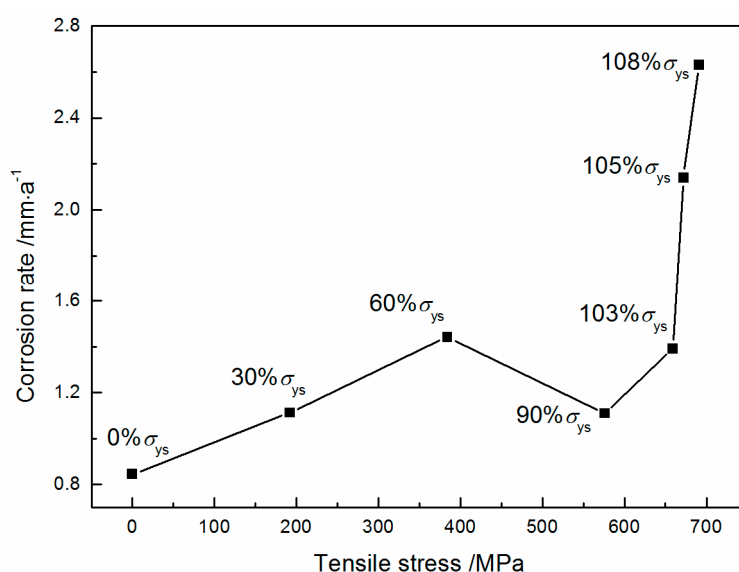


Figure 6. Corrosion rates of X80 steel exposed to 3.5 wt% NaCl aqueous solution with saturated CO₂ under different elastic and plastic tensile stress at 30 °C by fitting potentiodynamic polarization curves.

3.3. Electrochemical Impedance Spectroscopy

3.3.1. Anodic EIS

Figure 7a,b presents the Nyquist and Bode plots of X80 steel measured at +60 mV (vs. OCP) in 3.5 wt% NaCl aqueous solution with saturated CO₂ at 30 °C under elastic and plastic tensile stress, respectively. Each Nyquist plot in elastic stress range is composed of a capacitive loop at high frequency, an inductive loop, and a capacitive loop at low frequency. However, under plastic stress

conditions, the Nyquist plots do not have the capacitive loop in the low frequency range. In general, the capacitive loop at high frequency is associated with the electron transfer process on the surface as well as the charge-discharge process of electrical double layer between the electrode surface and electrolyte solution, while the data in the low frequency may be related to the adsorption of electrochemical reaction intermediates.

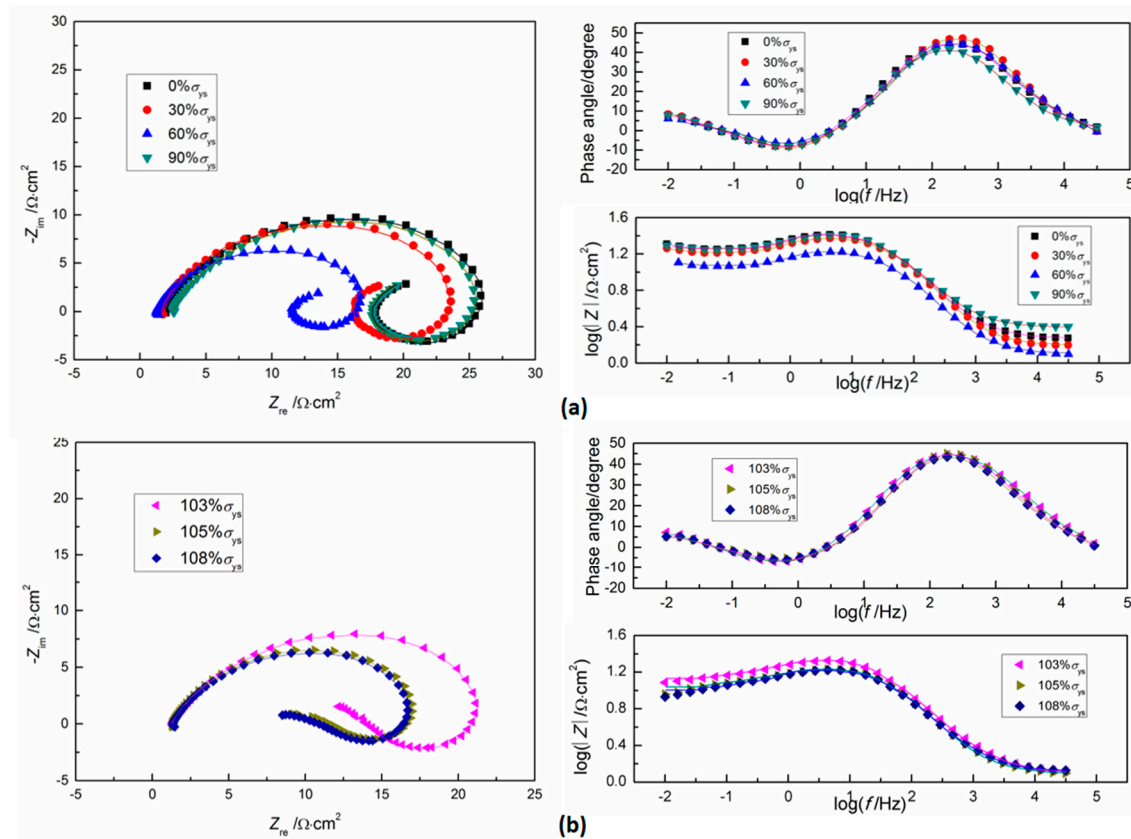


Figure 7. Electrochemical impedance spectroscopy (EIS) curves of X80 steel measured at +60 mV (vs. open-circuit potential, OCP) in 3.5 wt% NaCl aqueous solution with saturated CO₂ under different (a) elastic and (b) plastic tensile stress at 30 °C. Symbol: Experimental data; and line: Simulation data.

All the obtained EIS data for the X80 steel in the solution under elastic and plastic tensile stress were fitted to the equivalent circuit models as indicated in Figure 8a,b, respectively. In Figure 8, the $R_{s,a}$ is the aqueous solution resistance, $R_{t,a}$ the charge transfer resistance that occurs on the electrode surface, $R_{L,a}$ the resistance which may result from intermediate reactions on electrode surface. Generally, the electrical double layer is expressed as a capacitance component $C_{dl,a}$, but taking into account of the dispersion effect, a constant phase angle element (CPE_{dl,a}) $Q_{dl,a}$ is used to replace the $C_{dl,a}$ in the fitting procedure. The impedance of CPE_{dl,a} is expressed as [19]

$$Z_{CPE_{dl,a}} = \frac{1}{Y_{dl,a}(j\omega)^{n_{dl,a}}}, \tag{2}$$

where $Y_{dl,a}$ is the constant in $\Omega^{-1} \cdot \text{cm}^{-2} \cdot \text{s}^n$, $n_{dl,a}$ is the number constant between 0 and 1, and ω is the angular frequency. Thus, the total impedance of Figure 7a can be expressed by Equation (3), and that of Figure 7b by Equation (4):

$$Z = R_{s,a} + \frac{1}{Y_{dl,a}(j\omega)^{n_{dl,a}} + \frac{1}{R_{t,a} + \frac{1}{1/j\omega L_a + 1/R_{L,a}} + \frac{1}{j\omega C_a + 1/R_{C,a}}}}, \tag{3}$$

$$Z = R_{S,a} + \frac{1}{Y_{dl,a}(j\omega)^{n_{dl,a}} + \frac{1}{R_{t,a} + \frac{1}{1/j\omega L_a + 1/R_{L,a}}}}, \quad (4)$$

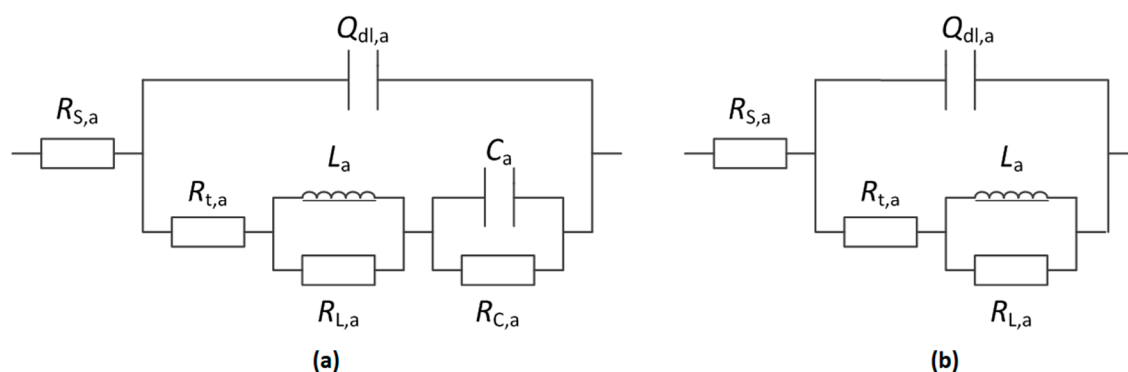


Figure 8. Equivalent circuit model for fitting the EIS measured at +60 mV (vs. OCP) under different (a) elastic and (b) plastic tensile stress at 30 °C.

According to the equivalent circuit models shown in Figure 8, the impedance spectra for the anodic dissolution of X80 steel have been fitted and some parameters are listed in Tables 3 and 4.

Table 3. Electrochemical impedance spectroscopy (EIS) parameters of X80 steel obtained by fitting the EIS curves of X80 steel measured at +60 mV (vs. OCP) in 3.5 wt% NaCl aqueous solution with saturated CO₂ under elastic tensile stress at 30 °C.

Tensile Stress	$R_{S,a}/\Omega \cdot \text{cm}^2$	$Y_{dl,a}/\Omega^{-1} \cdot \text{cm}^{-2} \cdot \text{s}^n$	$n_{dl,a}$	$R_{t,a}/\Omega \cdot \text{cm}^2$	$L_a/\text{H} \cdot \text{cm}^2$	$R_{L,a}/\Omega \cdot \text{cm}^2$	$C_a/\text{F} \cdot \text{cm}^{-2}$	$R_{C,a}/\Omega \cdot \text{cm}^2$
0	1.858	0.0005508	0.7866	16.30	1.5200	9.809	3.870	6.825
30% σ_{ys}	1.575	0.0004375	0.8186	14.95	1.3050	8.360	4.046	7.034
60% σ_{ys}	1.273	0.0007162	0.7938	10.65	0.8289	5.958	6.738	2.879
90% σ_{ys}	1.682	0.0005311	0.7905	15.51	1.3490	9.387	3.751	97.718

Table 4. EIS parameters of X80 steel obtained by fitting the EIS curves of X80 steel measured at +60 mV (vs. OCP) in 3.5 wt% NaCl aqueous solution with saturated CO₂ under plastic tensile stress at 30 °C.

Tensile Stress	$R_{S,a}/\Omega \cdot \text{cm}^2$	$Y_{dl,a}/\Omega^{-1} \cdot \text{cm}^{-2} \cdot \text{s}^n$	$n_{dl,a}$	$R_{t,a}/\Omega \cdot \text{cm}^2$	$L_a/\text{H} \cdot \text{cm}^2$	$R_{L,a}/\Omega \cdot \text{cm}^2$
103% σ_{ys}	1.308	0.0007835	0.7555	12.94	1.59	8.573
105% σ_{ys}	1.268	0.0006818	0.7937	10.25	1.274	6.282
108% σ_{ys}	1.355	0.0007329	0.7872	9.52	1.477	6.588

The charge transfer resistance $R_{t,a}$ listed in Tables 3 and 4 reflect the anodic reaction rate caused by tensile stress, that is, the larger the $R_{t,a}$, the lower the reaction rate. From the Tables, it can be seen that the value of $R_{t,a}$ first decreases and then increases with the increase of elastic tensile stress, and decreases in plastic stress state, which is consistent with the change tendency observed from the polarization curves.

3.3.2. Cathodic EIS

Figure 9 shows the Nyquist and Bode plots of the X80 steel measured at −60 mV (vs. OCP) in 3.5 wt% NaCl aqueous solution with saturated CO₂ at 30 °C under different tensile stress. Similar shapes of the Nyquist and Bode plots are observed from 0% σ_{ys} to 108% σ_{ys} , suggesting that the cathodic reactions of all samples follow the same mechanism, which is also supported by the polarization curves. As shown in Figure 9, each Nyquist plot consists of a high-frequency capacitance and a low-frequency line (Warburg impedance). The former is related to electron transfer and charge-discharge of double layer capacitance, and the latter is produced by the diffusion of cathode active species. According

to the electrochemical features of the cathodic polarization region and cathodic EIS of samples, it can be obtained that cathodic reaction process is mixed controlled by charge transfer and active species diffusion.

The impedance spectra were fitted by an equivalent circuit of Figure 10 where $R_{S,c}$ represents the resistance of the aqueous solution, $R_{t,c}$ the charge transfer resistance, $Q_{dl,c}$ the constant phase angle element used to replace $C_{dl,c}$, and $Z_{W,c}$ the Warburg impedance suggesting a diffusion-controlled reaction. The Warburg impedance $Z_{W,c}$ is expressed by Equation (5)

$$Z_{W,c} = A_{W,c}(j\omega)^{-0.5}, \quad (5)$$

where $A_{W,c}$ is the coefficient of $Z_{W,c}$. The total impedance of Figure 9 can be expressed by Equation (6).

$$Z = R_{S,c} + \frac{1}{Y_{dl,c}(j\omega)^{n_{dl,c}} + \frac{1}{R_{t,c} + Z_{W,c}}}, \quad (6)$$

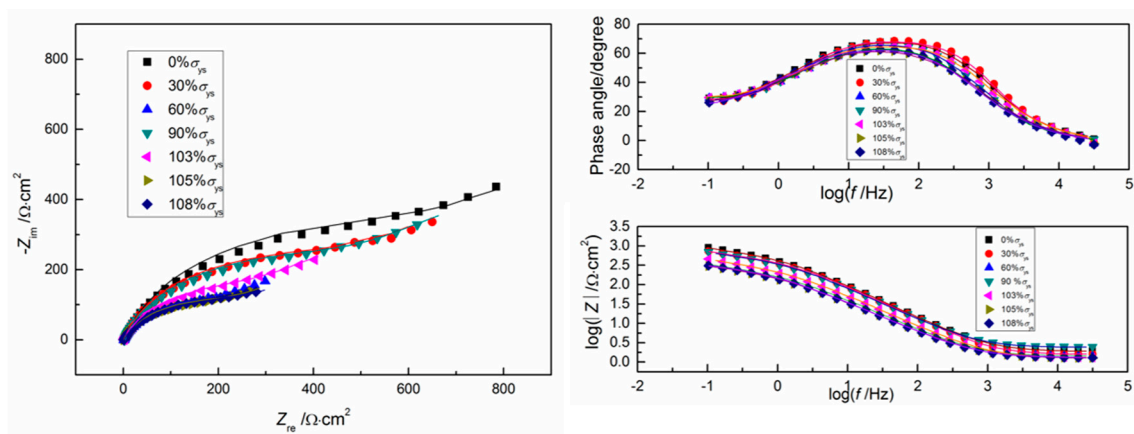


Figure 9. EIS curves of X80 steel measured at -60 mV (vs. OCP) in 3.5 wt% NaCl aqueous solution with saturated CO_2 under different elastic and plastic tensile stress at 30 °C. Symbol: Experimental data; Line: simulation data.

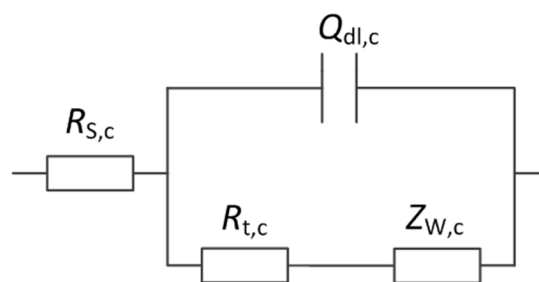


Figure 10. Equivalent circuit model for fitting the EIS measured at -60 mV (vs. OCP) under different elastic and plastic tensile stress at 30 °C.

Table 5 lists the fitted results of the impedance spectra in Figure 9. Here, $R_{t,c}$ reflects the cathodic reaction rate caused by tensile stress. Table 5 shows that the value of $R_{t,c}$ decreases from $573.3 \Omega \cdot \text{cm}^2$ at $0\% \sigma_{ys}$ to $228.0 \Omega \cdot \text{cm}^2$ at $60\% \sigma_{ys}$, then goes up to $519.2 \Omega \cdot \text{cm}^2$ at $90\% \sigma_{ys}$, while under plastic stress conditions it decreases from $260.7 \Omega \cdot \text{cm}^2$ at $103\% \sigma_{ys}$ to $196.9 \Omega \cdot \text{cm}^2$ at $108\% \sigma_{ys}$. While $R_{t,c}$ is not monotonously decreased with the increasing tensile stress, the $R_{t,c}$ s of all stressed samples are smaller than that without tensile stress, which means both the elastic and plastic tensile stress are able to enhance the cathodic reactions.

Table 5. EIS parameters of X80 steel obtained by fitting the EIS curves of X80 steel measured at -60 mV (vs. OCP) in 3.5 wt% NaCl aqueous solution with saturated CO_2 under different elastic and plastic tensile stress at 30 °C.

Tensile Stress	$R_{S,c} / \Omega \cdot \text{cm}^2$	$\gamma_{dl,c} / \Omega^{-1} \cdot \text{cm}^{-2} \cdot \text{s}^n$	$n_{dl,c}$	$R_{t,c} / \Omega \cdot \text{cm}^2$	$A_{W,c} / \Omega \cdot \text{cm}^2 \cdot \text{s}^{-0.5}$
0	1.914	0.0003185	0.8375	571.3	0.002394
$30\% \sigma_{ys}$	1.599	0.0003293	0.8463	465.5	0.003021
$60\% \sigma_{ys}$	1.449	0.0008707	0.8009	228.0	0.006291
$90\% \sigma_{ys}$	1.446	0.0003825	0.8295	474.6	0.003360
$103\% \sigma_{ys}$	1.319	0.0006090	0.8200	260.7	0.004155
$105\% \sigma_{ys}$	1.278	0.0001056	0.7876	212.0	0.007714
$108\% \sigma_{ys}$	1.314	0.0009652	0.8065	196.9	0.006539

3.4. Characterizations of Corroded Samples

Figure 11 presents the SEM photographs of corroded surface of X80 steel 3.5 wt% NaCl aqueous solution with saturated CO_2 under different elastic and plastic tensile stress. It is shown that without tensile stress (Figure 11a), several corrosion products are on the steel surface. Under elastic tensile stress range, a little more corrosion product is observed (Figure 11b–d). However, under plastic tensile stress range, not only corrosion products but also pits appear on the surface of the steel (Figure 11e–g), indicating that the surface activity of the samples under plastic tensile stress is higher than that under elastic tensile stress.

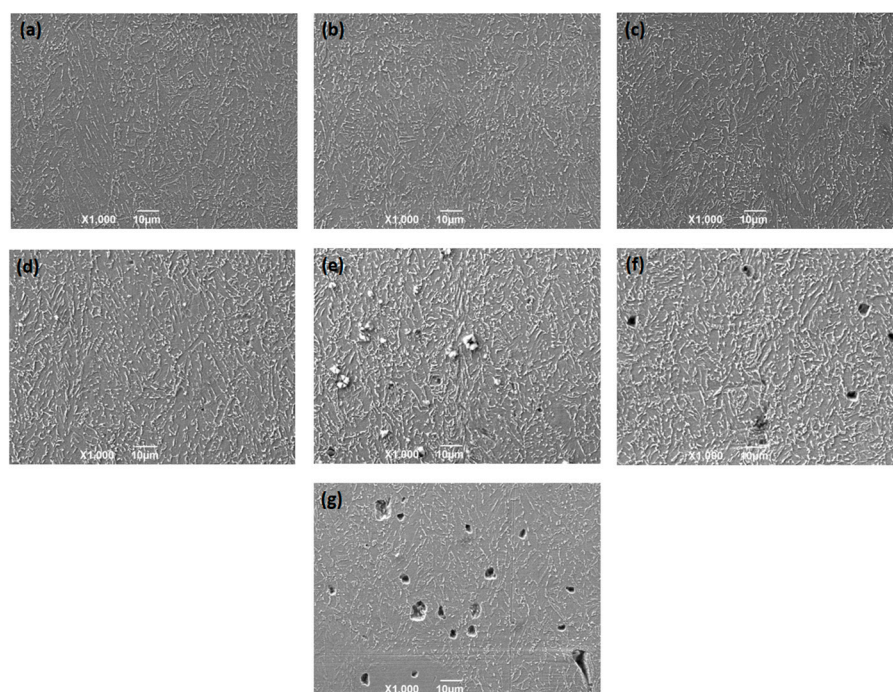


Figure 11. Scanning electron microscope (SEM) photographs of corroded surface of X80 steel in 3.5 wt% NaCl aqueous solution with saturated CO_2 at 30 °C under different tensile stress: (a) $0\% \sigma_{ys}$; (b) $30\% \sigma_{ys}$; (c) $60\% \sigma_{ys}$; (d) $90\% \sigma_{ys}$; (e) $103\% \sigma_{ys}$; (f) $105\% \sigma_{ys}$; and (g) $108\% \sigma_{ys}$.

4. Discussion

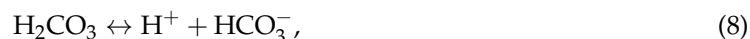
4.1. Electrochemical Reactions for CO_2 Corrosion

The experimental solution in this study is a typical CO_2 corrosion environment. As far as CO_2 corrosion goes, it is a complex process involving a number of chemical, electrochemical, and mass

transport processes [21]. When CO₂ is injected into an aqueous solution, it is first hydrated to generate a weak acid (H₂CO₃):



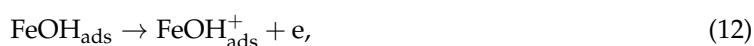
Then, the H₂CO₃ is dissociated in two steps:



which results in an acidic and corrosive solution. Subsequently, electrochemical corrosion reactions take place on the electrode surface, where the anodic reaction refers to the oxidation of iron:



There are several possible mechanisms proposed for explaining iron oxidation reaction in acidic media [2,22], where the consecutive mechanism proposed by Bockris et al. [23] has been commonly used to describe the anodic current in CO₂ corrosion of mild steel. In this study, the anodic polarization curves shown in Figure 5 have a Tafel slope (*b_a*) of around 40 mV (see Table 2), which is in accordance with the consecutive mechanism expressed by the reactions (11)–(13).



The rate-determining step for the consecutive mechanism is the reaction (12) in which the adsorption of the reaction intermediate FeOH_{ads} results in the low-frequency capacitance *C_a* and low-frequency inductance *L_a* of the anodic Nyquist plots, as shown in Figure 7.

For the CO₂ corrosion system, the cathodic reaction refers to the hydrogen evolution reaction which is a family of cathodic reactions that all have molecular hydrogen as their product, which contains the reduction of H⁺, H₂CO₃, HCO₃[−], and H₂O:



Reaction (14) is the most important cathodic reaction in an acidic solution. However, in the CO₂ system, the cathodic reaction is related to the CO₂ partial pressure and the pH value of the experimental solution [21]. At low pH (<4), reaction (14) is dominant owing to the high concentration of H⁺. When pH lies between 4 and 6, besides the H⁺ reduction, reaction (15) becomes important, and the total cathodic current is contributed by reactions (14) and (15) [24]. In this study, the pH value of the experimental solution was measured to be 4.0, which indicates that the reduction of H⁺ and H₂CO₃ are the main cathodic reactions. Therefore, the capacitance loop in the high-frequency zone in the cathodic Nyquist plots, as shown in Figure 9, reflects the electron transfer of H⁺ reduction and H₂CO₃ reduction as well as the charge-discharge of double layer capacitance. What is more, besides electron charge transfer, the mass transfer of H⁺ and H₂CO₃ has an important influence on cathodic current of reactions (14) and (15), which gives rise to a deviation from cathodic Tafel behavior, as shown in Figure 9, and brings the Warburg impedance in the low-frequency zone in the cathodic Nyquist plots (see Figure 9).

4.2. Mechanoelectrochemical Effect

According to the mechanoelectrochemical theory proposed by Gutman [25], the applied load can affect the electrochemical properties of the electrode. The change of equilibrium electrochemical potential by applied load is expressed as follows [25]

$$\Delta\varphi_e^0 = -\frac{\Delta PV_M}{zF}, \quad (18)$$

where P is the excess pressure (Pa), V_M is the molar volume of metal ($\text{m}^3 \cdot \text{mol}^{-1}$), and z is the number of transferred electron. This equation indicates that an applied load would decrease the potential of the steel and increase its electrochemical thermodynamic activity.

When the tensile stress reaches the plastic zone, the plastic stress leads to the appearance of the dislocation pile-up group at the barrier through the movement and proliferation of dislocation, which would affect the electrode potential by the following equation [25,26]:

$$\Delta\varphi_p^0 = -\frac{n\Delta\tau R}{\bar{\alpha}kN_{\max}zF}, \quad (19)$$

where $\Delta\varphi_p^0$ is the change in equilibrium potential owing to plastic deformation of the electrode, $\Delta\tau$ reflects the extent of work hardening, numerically equaling the residual stress caused by dislocations, n is the number of dislocation in a dislocation pile-up, R is the ideal gas constant, k is the Boltzmann constant, $\bar{\alpha}$ is the average dislocation density, and N_{\max} is the maximal number of dislocation in unit volume. It is a big challenge to calculate the $\Delta\varphi_p^0$ by Equation (19), since the parameters involved in Equation (19) are difficult to be measured accurately in experiment. However, based on this equation, it is undoubted that with the increase of the plastic stress, the number of dislocations increases, and as a result, the electrode potential decreases and the steel corrosion is enhanced.

In this study, a negative shift of corrosion potential is observed in both elastic and plastic regions, as shown in Figure 4; moreover, the potential in the plastic stress region is more negative than that in the elastic stress region, which indicates the electrochemical corrosion activity of the steel was improved by the tensile stress, and plastic stress is more significant for corrosion activity compared with elastic stress.

4.3. Corrosion of Stressed Pipeline Steels in CO₂ Environment

According to the above analysis, we attempted to describe, qualitatively, the corrosion behavior of X80 steel under tensile stress in CO₂ environment. Figure 12 shows the schematic diagram of the possible corrosion process of stressed X80 steel in CO₂ environment. Without applied stress, the corrosion process of the steel is just controlled by the combination of cathodic charge transfer and active species diffusion (Figure 12a). Under elastic tensile stress, stress would take effect according to mechano-electrochemical theory. At relatively low tensile stress, only a few dislocation in the steel start to move by tensile stress, which does not affect the corrosion process, but with the increase of tensile stress, the edge dislocation would appear on the steel surface, which results in the increases of the active sites on the surface (Figure 12b). At very high elastic stress (i.e., 90% σ_{ys} in this study), the pre-existing dislocation pile-up in the steel would be relaxed and no new ones formed [18], therefore, the corrosion activity of the steel slightly decreases (Figure 12c) and hence its corrosion morphology is not obviously different from that at other elastic stress states (Figure 11c,d). In general, elastic tensile stress has a limited effect on the corrosion of X80 steel. However, under plastic tensile stress conditions, slipping begins to take place and several slip planes emerge at the surface of steel, which largely increases the corrosion activity of the steel surface. The active dissolution would preferentially occur from local areas of exit of slip planes, as a result, the corrosion is significantly accelerated (Figure 12d).

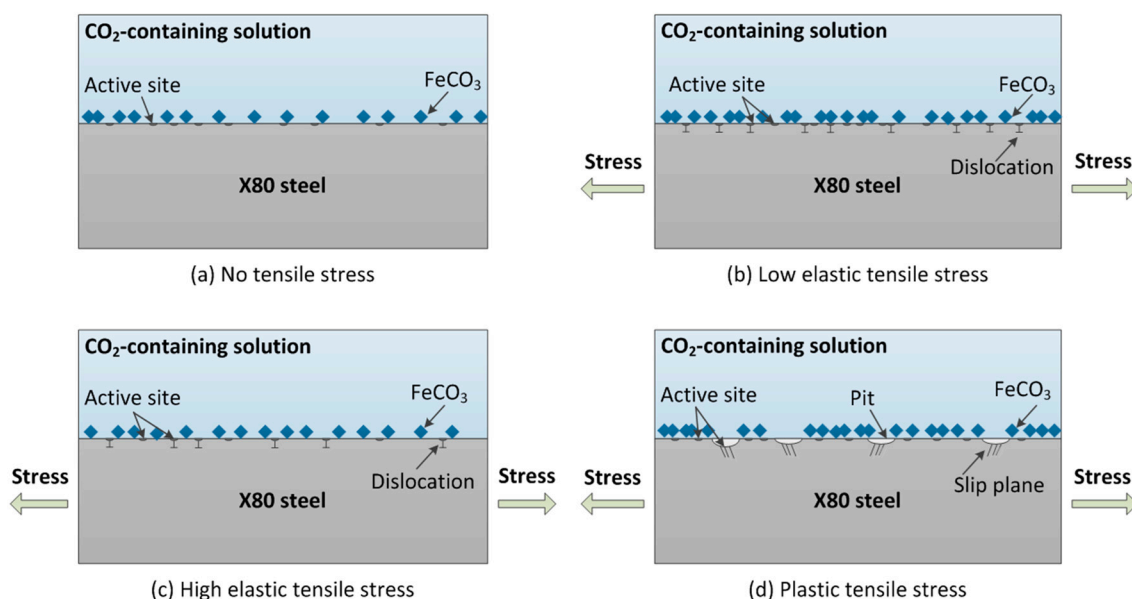


Figure 12. Schematic of corrosion of stressed X80 steel in CO₂ environment.

5. Conclusions

- (1) Corrosion rate of stressed X80 steel in 3.5 wt% NaCl aqueous solution with saturated CO₂ at 30 °C increases from 0.845 mm·a⁻¹ at 0%σ_{ys} to 1.442 mm·a⁻¹ at 60%σ_{ys}, and then slightly decreases to 1.110 mm·a⁻¹ at 90%σ_{ys} due to partial stress relaxation and dislocation annihilation at very high elastic stress. In the plastic stress range, corrosion rate increases sharply up to 2.631 mm·a⁻¹ at 108%σ_{ys}, which is about three times higher than that without tensile stress.
- (2) Both elastic tensile stress and plastic tensile stress can decrease the electrode potential and improve the electrochemical corrosion activity of X80 steel in CO₂-saturated NaCl aqueous solution. Moreover, plastic tensile stress has a more significant effect than elastic tensile stress.
- (3) According to potentiodynamic polarization and EIS analysis, both anodic and cathodic reactions are accelerated by tensile stress.
- (4) According to the mechano-electrochemical theory, the corrosion of stressed X80 steel is significantly affected by the surface activity, which has much to do with the microscopic defect (like dislocation and slip plane) on the surface caused by tensile stress.

Author Contributions: W.W. proposed this research idea, design the experimental scheme and drafted the article. H.Y., H.Z. and J.K. conducted electrochemical tests. Y.L. and Y.D. conducted the analysis and interpretation of experimental data. All authors read and approved the final manuscript.

Funding: This research was funded by the National Natural Science Foundation of China, grant numbers 51605368 and 21576224.

Conflicts of Interest: The authors declare no conflict of interest.

References

1. Liang, P.; Li, X.; Du, C.; Chen, X. Stress corrosion cracking of X80 pipeline steel in simulated alkaline soil solution. *Mater. Des.* **2009**, *30*, 1712–1717. [[CrossRef](#)]
2. Nešić, S. Key issues related to modelling of internal corrosion of oil and gas pipelines—A review. *Corros. Sci.* **2007**, *49*, 4308–4338. [[CrossRef](#)]
3. Song, F.M. A comprehensive model for predicting CO₂ corrosion rate in oil and gas production and transportation systems. *Electrochim. Acta* **2010**, *55*, 689–700. [[CrossRef](#)]
4. Eliyan, F.F.; Mahdi, E.S.; Alfantazi, A. Electrochemical evaluation of the corrosion behaviour of API-X100 pipeline steel in aerated bicarbonate solutions. *Corros. Sci.* **2012**, *58*, 181–191. [[CrossRef](#)]

5. Xue, H.B.; Cheng, Y.F. Passivity and pitting corrosion of X80 pipeline steel in carbonate/bicarbonate solution studied by electrochemical measurements. *J. Mater. Eng. Perform.* **2010**, *19*, 1311–1317. [[CrossRef](#)]
6. Mohammadi, F.; Eliyan, F.F.; Alfantazi, A. Corrosion of simulated weld HAZ of API X-80 pipeline steel. *Corros. Sci.* **2012**, *63*, 323–333. [[CrossRef](#)]
7. Wang, Y.; Cheng, G.X.; Wu, W.; Qiao, Q.; Li, Y.; Li, X.F. Effect of pH and chloride on the micro-mechanism of pitting corrosion for high strength pipeline steel in aerated NaCl solutions. *Appl. Surf. Sci.* **2015**, *349*, 746–756. [[CrossRef](#)]
8. Kermani, M.B.; Morshed, A. Carbon dioxide corrosion in oil and gas Production—A compendium. *Corrosion* **2013**, *59*, 659–683. [[CrossRef](#)]
9. Eduok, U.; Ohaeri, E. Electrochemical and surface analyses of X70 steel corrosion in simulated acid pickling medium: Effect of poly (N-vinyl imidazole) grafted carboxymethyl chitosan additive. *Electrochim. Acta* **2018**, *278*, 302–312. [[CrossRef](#)]
10. Eduok, U.; Jossou, E.; Szpunar, J. Enhanced surface protective performance of chitosanic hydrogel via nano-CeO₂, dispersion for API 5L X70 alloy: Experimental and theoretical investigations of the role of CeO₂. *J. Mol. Liq.* **2017**, *241*, 684–693. [[CrossRef](#)]
11. Ohaeri, E.; Omale, J.; Eduok, U.; Szpunar, J. Effect of Thermomechanical Processing and Crystallographic Orientation on the Corrosion Behavior of API 5L X70 Pipeline Steel. *Metall. Mater. Trans. A* **2018**, *49*, 2269–2280. [[CrossRef](#)]
12. Xu, L.Y.; Cheng, Y.F. An experimental investigation of corrosion of X100 pipeline steel under uniaxial elastic stress in a near-neutral pH solution. *Corros. Sci.* **2012**, *59*, 103–109. [[CrossRef](#)]
13. Xu, L.Y.; Cheng, Y.F. Corrosion of X100 pipeline steel under plastic strain in a neutral pH bicarbonate solution. *Corros. Sci.* **2012**, *64*, 145–152. [[CrossRef](#)]
14. Boven, G.V.; Chen, W.; Rogge, R. The role of residual stress in neutral pH stress corrosion cracking of pipeline steels. Part I: Pitting and cracking occurrence. *Acta Mater.* **2007**, *55*, 29–42. [[CrossRef](#)]
15. Bao, M.; Ren, C.; Lei, M.; Wang, X.; Singh, A.; Guo, X. Electrochemical behavior of tensile stressed P110 steel in CO₂ environment. *Corros. Sci.* **2016**, *112*, 585–595. [[CrossRef](#)]
16. Li, M.C.; Cheng, Y.F. Corrosion of the stressed pipe steel in carbonate–bicarbonate solution studied by scanning localized electrochemical impedance spectroscopy. *Electrochim. Acta* **2008**, *53*, 2831–2836. [[CrossRef](#)]
17. Li, K.; Wu, W.; Cheng, G.X.; Li, Y.; Hu, H.J.; Zhang, H. Corrosion behavior of X70 pipeline steel and corrosion rate prediction under the combination of corrosive medium and applied pressure. In Proceedings of the ASME 2017 Pressure Vessels and Piping Conference, Waikoloa, HI, USA, 16–20 July 2017.
18. Wang, Y.; Zhao, W.; Ai, H.; Zhou, X.; Zhang, T. Effects of strain on the corrosion behaviour of X80 steel. *Corros. Sci.* **2011**, *53*, 2761–2766. [[CrossRef](#)]
19. Lasia, A. *Electrochemical Impedance Spectroscopy and Its Applications*; Springer: New York, UK, 2014; ISBN 978-1461489320.
20. Bard, A.J.; Faulkner, L.R. *Electrochemical Methods: Fundamentals and Applications*, 2nd ed.; John Wiley & Sons: New York, UK, 2001; ISBN 978-0471043720.
21. Nordsveen, M.; Nešić, S.; Nyborg, R.; Stangeland, A. A mechanistic model for carbon dioxide corrosion of mild steel in the presence of protective iron carbonate films—Part 1: Theory and verification. *Corrosion* **2012**, *59*, 616–628. [[CrossRef](#)]
22. Liu, Q.Y.; Mao, L.J.; Zhou, S.W. Effects of chloride content on CO₂ corrosion of carbon steel in simulated oil and gas well environments. *Corros. Sci.* **2014**, *84*, 165–171. [[CrossRef](#)]
23. Bockris, J.O.; Drazic, D.; Despic, A.R. The electrode kinetics of the deposition and dissolution of iron. *Electrochim. Acta* **1961**, *4*, 325–361. [[CrossRef](#)]
24. Nešić, S.; Postlethwaite, J.; Olsen, S. An electrochemical model for prediction of corrosion of mild steel in aqueous carbon dioxide solutions. *Corrosion* **1996**, *52*, 280–294. [[CrossRef](#)]
25. Gutman, E.M. *Mechanochemistry of Materials*; Cambridge International Science Publishing: Cambridge, UK, 1998; ISBN 1-898326-32-0.
26. Xu, L.Y.; Cheng, Y.F. Development of a finite element model for simulation and prediction of mechano-electrochemical effect of pipeline corrosion. *Corros. Sci.* **2013**, *73*, 150–160. [[CrossRef](#)]

